Direct growth of metallic single-metal-atom chains

Shasha Guo[1]†, Jiecai Fu[2,8]†, Peikun Zhang[3]†, Chao Zhu[1,7]†, Heming Yao[5], Manzhang Xu[1], Boxing An[6], Xingli Wang[14], Bijun Tang[1], Ya Deng[1], Teddy Salim[1], Hongchu Du[2,9], Rafal E. Dunin-Borkowski[2], Mingquan Xu[10], Wu Zhou[10], Beng Kang Tay[13, 14], Chao Zhu[1], Yanchao He[1], Mario Hofmann[11], Ya-Ping Hsieh[12], Wanlin Guo[3], Michael Ng[5], Chunlin Jia[2]*, Zhuhua Zhang[3]*, Yongmin He[1,4]*, and Zheng Liu[1, 13, 14]*

[1] School of Materials Science and Engineering, Nanyang Technological University; Singapore 639798, Singapore.

[2] Ernst Ruska-Centre for Microscopy and Spectroscopy with Electrons and Peter Grünberg Institute, Forschungszentrum Jülich GmbH; Jülich 52425, Germany.

[3] State Key Laboratory of Mechanics and Control of Mechanical Structures, Key Laboratory for Intelligent Nano Materials and Devices of Ministry of Education, and Institute for Frontier Science, Nanjing University of Aeronautics and Astronautics; Nanjing 210016, China

[4] State Key Laboratory of Chemo/Biosensing and Chemometrics, College of Chemistry and Chemical Engineering, Hunan University; Changsha 410082, China.

[5] Department of Mathematics, The University of Hong Kong; Hong Kong 999077, China

[6] College of Materials Science and Engineering, Beijing University of Technology; Beijing 100124, China.

[7] SEU-FEI Nano-Pico Center, Key Lab of MEMS of Ministry of Education, School of Electronic Science and Engineering, Southeast University, Nanjing 210096, China

[8] Key Laboratory for Magnetism and Magnetic Materials of the Ministry of Education, School of Physical Science and Technology, Lanzhou University; Lanzhou 730000, China

[9] Central Facility for Electron Microscopy, RWTH Aachen University; Aachen 52074, Germany

[10] School of Physical Sciences, CAS Key Laboratory of Vacuum Physics, University of Chinese Academy of Sciences; Beijing, 100049, China

[11] Department of Physics, National Taiwan University; Taipei 10617, Taiwan.

[12] Institute for Atomic and Molecular Sciences, Academia Sinica; Taipei 10617, Taiwan.

[13] School of Electrical and Electronic Engineering, Nanyang Technological University; Singapore 639798, Singapore

[14] CINTRA CNRS/NTU/THALES, UMI 3288, Research Techno Plaza; Singapore 639798, Singapore

†Shasha Guo, Jiecai Fu, Peikun Zhang, and Chao Zhu contributed equally to this work.

* Corresponding author. E-mail: c.jia@fz-juelich.de, chuwazhang@nuaa.edu.cn, ymhe@hnu.edu.cn, and z.liu@ntu.edu.sg

Abstract:

Single-metal-atom chains (SMACs), as the smallest one-dimensional structure, have intriguing physical and chemical properties. Although several SMACs have been realized to date, their controllable fabrication remains challenging, because of the need to arrange single atoms in an atomically precise manner. Here, we develop a chemical vapour co-deposition method to construct a wafer-scale network of Pt SMACs in atom-thin films. The obtained atomic chains possess an average length of up to ~17 nm and a high density of over 10 wt%. Interestingly, as a consequence of the electronic delocalization of Pt atoms along the chain, this atomically coherent one-dimensional channel delivers a metallic behaviour, as revealed by electronic measurements, first-principles calculations, and complex network modelling. Our strategy is potentially extendable to other transition metals, e.g., Co, enriching the toolbox for manufacturing SMACs and paving the way for the fundamental study of one-dimensional systems and the development of monoatomic chain devices.

Introduction: Single-metal-atom chains (SMACs), known as one of the smallest one-dimensional structures, have garnered broad research interest, attributing to their unique properties, such as quantized conductance, thermal transport, charge/spin density waves, and peculiar magnetic properties, as well as distinct catalytic properties.[1-6] For example, it was reported that the average bond strength in the chain is twice that of the bulk counterpart[7]. Up to now, several SMACs like Au, Ir, and Pt chains have been fabricated by using a top-down mechanical break junction (MBJ) method, showing quantum ballistic transport[8, 9], anisotropic magnetoresistance[10, 11], and the Kondo effect[12]. Alternatively, an ultra-high vacuum (UHV) self-assembly approach on the ultra-clean substrate was developed for preparing Au SMACs on Si, and Ge stepped surfaces[13-15], serving as a 1D model system to study Peierls instabilities and Tomonaga–Luttinger liquid. Unfortunately, these methods require harsh growth conditions. Besides, the MBJ-SMACs suffer from low consecution (< 5 atoms length) and structural fragility, whereas self-assembled atom wires are extremely unstable under the atmosphere. These characteristics significantly restrict the broad applicability of resultant SMACs, particularly in devices[16]. Therefore, exploring a simple and efficient strategy for the scalable synthesis of SMACs with ambient atmosphere stability is still highly demanded to date.

Inspired by the formation mechanism of the 1D grain-boundary (GB) channel in 2D materials[17-20], we here report the fabrication of Pt SMACs network within the transition-metal dichalcogenide material (TMDC) film at a wafer scale (5 centimetres). The mirror-twin grain-boundary (MTB) acts as an ideal 1D host for Pt atoms, and the obtained Pt SMACs possess an average length of up to 17 nm and remarkable ambient air stability. We further demonstrate that these Pt SMACs are highly metallic, forming a network conduction pathway in the 2D film to enrich their electronic properties and functionalities. Moreover, we have also embedded Co

SMACs into MTBs of the MoS_2 film, suggesting the generalizability of our strategy for wafer-scale production of ambient air-stable SMACs.

Results and discussion

Synthesis and characterization of Pt SMACs. A chemical vapor co-deposition method was developed to fabricate Pt SMACs network in a wafer-scale atomically thin MoS_2 film (Fig. 1a) (see Methods for details). Ultra-small Pt nanoclusters (0.5-2 nm) were pre-deposited on SiO_2/Si substrate through e-beam evaporation, followed by the growth of MoS_2. This pre-deposited Pt layer plays two crucial roles in forming Pt SMACs: (i) serving as nucleation sites to induce the formation of GB-rich MoS_2 film (Fig. 1b). Highly dense Pt nanoclusters with an average spacing down to a few nanometers can be obtained by using low-rate evaporation (0.1 Å s^{-1}) in our experiment (Supplementary Fig. 1-2). It enables the growth of high-density MoS_2 nanograins that provide abundant 1D channels for the Pt atom incorporation (Supplementary Fig. 8); (ii) supplying Pt to form Pt SMACs. As shown in Fig. 1e, these ultra-small Pt nanoclusters tend to become a liquid phase at the growth temperature of MoS_2 (600-750°C)[21]. Such liquid nanodroplets facilitate the diffusion of Pt atoms, which are further captured by MoS_2 domains to form thermodynamically stable structures. In short, Pt nanoclusters drive the growth of the GB-rich MoS_2 film. These dense GBs provide anchor sites for mobile Pt atoms, yielding single-atom-chain structures. Fig. 1b presents as-grown Pt SMACs in wafer-scale MoS_2 film from macroscopic to atomic views.

Next, we used X-ray photoelectron spectroscopy (XPS) and Raman spectroscopy to investigate the bonding states and the detailed structure of Pt SMACs. As shown in Fig. 1c, two sets of Pt(II) peaks can be clearly observed in the Pt 4f region, which correspond to two kinds of Pt(II) in different chemical environments. The absence of metallic Pt peaks indicates that all Pt

atoms are covalently bonded with S atoms instead of being physically adsorbed on the MoS_2 surface nor isolated as particles. Furthermore, large-area XPS analysis reveals an average Pt mass loading as high as ~13 wt%, implying a high density of SMACs achieved by this method. Notably, the mass loading achieved in our work is much higher than that of atomically dispersed Pt atoms (~5 wt%) in other works. Fig. 1d presents the Raman spectra of as-grown films. Given that the in-plane to out-of-plane mode ratio is a widely adopted metric to evaluate the crystallinity of MoS_2, our sample has a much smaller intensity ratio (0.28) than currently reported CVD-grown (~1.89) and physically exfoliated (~1.57) samples (Supplementary Table 1), suggesting a polycrystalline nature with high-density GBs. After examining tens of regions, we hardly observe peaks associated with PtS_2 or PtS, thus confirming that most Pt atoms are covalently bonded with S atoms at MoS_2 MTB instead of forming PtS_2 or PtS particles, which also agrees with the above XPS results.

We then examined the atomic structure of Pt SMACs in the monolayer MoS_2 film using annular dark-field scanning transmission electron microscopy (ADF-STEM) imaging, wherein Pt atoms with a high Z-contrast could be clearly identified (Fig. 2a). The corresponding fast-Fourier transformation pattern (viewing from the zone axis of <001> in the inset of Fig. 2a) presents a diffraction spot configuration of hexagonal arrangement, confirming the formation of 60-degree-rotation inversion domains. It can be seen that the majority of Pt atoms exactly reside at the MTB to form a single chain. In addition, a small amount of dispersed Pt atoms are also observed in our sample, which is due to the filling of Pt atoms in native vacancies inevitably introduced during the CVD process[22, 23], to minimize the system energy. To probe the local environment surrounding the Pt atoms, we examined the blue rectangular region highlighted in Fig. 2a. It turns out that Pt atoms form an atomically coherent 1D channel at the twin boundary (60°) (Fig. 2b), which agrees well with the simulated results in Fig. 2c. The corresponding intensity profiles

along Pt SMACs indicate that the distance between adjacent Pt atoms is around 3.2 Å (Fig. 2d), much larger than the conventional Pt-Pt bonds, *i.e.*, 2.78 Å in the (111) plane[24, 25]. The above observations suggest a unique structure of our highly ordered Pt single-atom-chain (see its detailed model within monolayer MoS_2 in Fig. 2e).

Geometric phase analysis (GPA) was also implemented on the ADF-STEM to draw the strain fields of these SMACs in Fig. 2f (see Methods section). The MoS_2 lattice parameter was selected as the reference. An apparent compressive strain around the two sides of the Pt SMAC is observed along the x-axis (ε_{xx}, the perpendicular direction to SMAC), but negligible along the *y*-axis (ε_{yy}, the parallel direction to Pt SMAC). We note that the ε_{xx} compressive strain is as high as 5.5 ± 1.1%, indicating an effective uniaxial SMAC-localized in-plane strain.

To study the possible interlayer influence between Pt SMACs and MoS_2 layer, we examined the SMAC's structure in bilayer MoS_2. Upon applying the false-colour treatment on STEM images, the typical 3R and 2H stacking registries become distinguishable through the weak atom blobs in each honeycomb. As shown in Fig. 3a, Pt SMACs mainly present at a lateral 3R|2H|3R hybrid structure in bilayer MoS_2, which has a stacking sequence of AB|AA′|BA[26]. Intriguingly, we found two types of Pt SMAC structures in bilayer MoS_2: Pt atoms in the bottom layer (Fig. 3b) and the top layer (Fig. 3c). The latter usually shows a brighter contrast than that of the former in the STEM imaging. The corresponding intensity profiles can be used to distinguish them (see right panels in Fig. 3b-c)**.** We also applied GPA to probe the strain distribution around Pt SMACs in bilayer MoS_2 (Fig. 3d). It exhibits a phenomenon similar to that of monolayer MoS_2 (Fig. 2f), with a stronger compressive strain along the *x*-axis than that along the *y*-axis. Note that, in bilayer MoS_2, the formed strain around the Pt SMAC is significantly averaged in both the

bottom and top layers, thus exhibiting a weaker strain phase profile than that of the monolayer counterpart.

Formation mechanism. To elucidate the formation mechanism of Pt SMACs, we carried out the density functional theory (DFT) calculations (see details in Methods). First, by comparing the formation energy of a set of Pt-MoS_2 systems, we searched for the energy-optimal geometry for Pt atoms attached to the MoS_2 lattice. Among the enumerated structures, a four-coordinated motif (Pt-S_4), in which the single Pt atom covalently bond with 4 S atoms at the edge of MoS_2, gives the lowest binding energy (Supplementary Fig. 13). Such structure is also confirmed by our high-resolution characterization of the MoS_2 edge (Fig. 4a, bottom). Upon the chemisorption of several Pt atoms, we note that the energetically most favorable configuration is an ordered array of adjacent Pt-S_4 motifs at the MoS_2 terminal-end (Supplementary Fig. 14). Second, we explored the possible dynamical evolution of the adsorbed Pt atoms during the growth of a MoS_2 domain. In our calculations, MoS_2 units were added step-by-step to the Pt-terminated zigzag edge. At each step, various Pt attached sites were examined to ensure the optimal configuration (see configurational spectra at each growth step in Supplementary Fig. 16). These results indicate that the configurations that seamlessly extend the MoS_2 lattice are in low energy regions. The evolution of atomic configurations along the lowest energy pathway is presented in Fig. 4a, manifesting the flow of kinks along the Pt-passivated edge. In brief, the Pt-S_4 motif first evolves into a new kink hexagon (Fig. 4a ii) and later into a MoS_2 hexagon (Fig. 4a iii), which is also experimentally evidenced at a domain edge (Figure 4a, bottom). Later, the Continuous feeding of Mo and S atoms moves the kink to complete the growth of a new row, resulting in one-MoS_2 lattice-constant migration of the Pt-terminated edge along the growth direction (Fig. 4a vii). Therefore, we here call this dynamical evolution the "surfing" of Pt atoms, that is, the Pt-S_4 motifs will migrate to the growth front during the growing process.

Based on the above calculations, Pt atoms could "zip" them together by keeping the Pt-S_4 motifs, when two inversely oriented domains with similar Pt-termination connect laterally. This process yields a chain of Pt atoms covalently embedded in the MTB, namely, Pt SMAC (Fig. 4b). *Ab initio* molecular dynamics simulations suggest that the chain has excellent structural stability and can sustain an elevated temperature as high as 1000 K (Supplementary Fig. 19). We also studied the energy-optimized structure of Pt SMACs in a bilayer MoS_2 using MD simulations, showing that Pt SMACs are formed at the GBs between 2H and 3R phased bilayer MoS_2 (Supplementary Fig. 15), in good agreement with the atomic structure shown in Fig. 3b-c.

Metallic behaviour of Pt SMACs. The highly ordered Pt SMACs possess a larger interatomic distance than Pt metal (3.2 Å vs. 2.78 Å), determined by the host MoS_2 MTB. To examine the possible interaction in Pt SMACs, we further investigate the partial charge density distribution of Pt 5d orbitals (the inset of Fig. 4b). Apart from localized bonding electrons between S and Pt atoms, we also note substantial delocalized electron densities between adjacent Pt atoms, rendering SMACs as electronic transport channels. We then calculated the band structure and projected density of states (PDOS) of the SMACs, confirming the metallic behaviour (Fig. 5a and b, Supplementary Fig. 20, the red dot line) in sharp contrast to the scattered Pt atoms. This metallic behaviour is attributed to the substantial overlap of Pt electronic states, stemming from the Pt-Pt spacing less than 0.9 nm in our Pt SMACs. On the contrary, Pt atoms with a neighbour distance exceeding 1.5 nm (*e.g.*, single scattered Pt atoms) possess a highly localized defect band level, hindering the electronic transport (Supplementary Fig17). Electron localization function (ELF) further supports this result from the covalent interaction between Pt and S atoms (Supplementary Fig. 21) as well as electronic delocalization between Pt atoms along the chain (Fig. 5c). Moreover, charge transfer analysis between two stacked MoS_2 layers indicates that Pt

atoms in the top MoS_2 layer donate electrons to S atoms in the bottom MoS_2 layer (Fig. 5d), which is in good accordance with the two types of Pt (II) signals in the XPS spectra (Fig. 1c).

To verify this metallic behaviour of Pt SMACs, we fabricated a series of FET devices with channel lengths ranging from 2 μm down to 50 nm. The channel width kept constant at 1 μm (Fig. 5e and Supplementary Fig. 22). It is observed that the resistivity of the sample is around two orders of magnitude lower than that of CVD-grown MoS_2 (Fig. 5f, Supplementary Fig. 24).[27, 28] Moreover, the resistivity exhibits an initial linear increase and later a critical transition from high to low value, demonstrating a volcanic relationship with the channel length (*l*). To further elaborate on this phenomenon, we adopt the complex-network-based method, a powerful tool for simulating carrier transport in nanostructured film[29-31], to investigate the electronic transport behaviour of Pt SMACs within MoS_2 film. The trend of the calculated resistivity shows a length dependence, well-consistent with the experimental results (Fig. 5h). Furthermore, the visualization of the current distribution confirms that carrier conduction proceeds by percolation through the Pt atomic chains for all length scales (Fig. 5g). Specifically, i) at shorter channel lengths (region 1), the termination of percolative pathways[32] causes the increased resistivity; ii) at longer channel lengths (region 2), the high density of Y-shaped Pt SMACs junctions, which are formed due to the merging of MoS_2 grains, significantly enhances the conductivity of the channel (See Supplementary Note 2 for detailed discussion). Expectedly, our one-dimensional metallic chains can provide a model system to study interacting electrons, such as Tomonaga–Luttinger liquid and charge density waves[33-36].

Conclusion

In summary, we developed a facile and effective chemical vapor co-deposition strategy to fabricate a wafer-scale network of Pt SMACs with remarkable stability. The atomic structures

and electronic properties of Pt SMACs were extensively studied in monolayer and bilayer MoS_2 films. Combining DFT analysis with experimental results, we proposed a "surf-zip" growth mechanism to reveal the growth process of Pt SMACs, and later successfully extended to grow Co SMACs via our co-deposition method (Supplementary Fig. 18). Moreover, we found a metallic behaviour of Pt SMACs originated from the substantial overlap of Pt electronic states, which can facilitate the electronic conduction of atom-thin films via the percolation through SMAC networks. Finally, our work offers a promising route to fabricate air-stable SMACs on a large-scale, and provides one of the smallest one-dimensional platforms for studying Luttinger liquids, the Fermi-liquid microscopic model, and other theoretical 1D models.

Methods

Synthesis of wafer-scale Pt SMACs inside MoS_2 films. 1) The Pt films were deposited on clean SiO_2/Si or sapphire wafers using e-beam evaporation with a speed of 0.1 Å s^{-1} for 10 s. 2) The as-prepared Pt-coated SiO_2/Si wafers were used as the substrates for the chemical vapor deposition (CVD) of MoS_2 films (Supplementary Fig. 3). To be more precise, the substrates were placed facing down on an aluminum oxide boat containing MoO_3 powders in the middle of a quartz tube reaction chamber, and sulfur powders were loaded in another crucible upstream in the tube. 3) After purging the CVD system by 500 standard cubic centimetres per minute (sccm) argon flow for 3 min, the center of the furnace was heated from room temperature to growth temperature with a ramp of ~50 °C min^{-1} under continuous argon gas of 60 sccm. The Pt SMACs inside MoS_2 films were synthesized by keeping the temperature of Mo sources at 650 °C for 4 mins, while S sources at around 230 °C. 4) The furnace was naturally cooled down under the protective argon atmosphere.

Material characterization Raman spectra were collected on a Renishaw inVia microscope under 532 nm laser at room temperature. The spot size is about 1 μm in diameter. The chemical states of obtained samples were analyzed by X-ray photoelectron spectroscopy (Kratos AXIS Supra XPS with a monochromatic Al-Kα source). Peak positions were all corrected by the C 1s spectrum at 284.8 eV.

STEM-ADF imaging and analysis. The as-prepared samples on the SiO_2/Si or sapphire wafers were transferred to the TEM grid for the STEM characterizations with the mediator of polymethyl methacrylate (PMMA). To avoid the hydrocarbon contamination during electron microscopy studies, all the TEM samples were baked at 200 °C for 8 hours under vacuum before the microscopy experiment. And ADF-STEM imaging and EDS mapping were conducted using

an aberration-corrected FEI ChemiSTEM operated at 200 kV with an approximately 20 pA probe current. The high signal-to-noise ratio ADF-STEM images are obtained by an image series composed of thirty fast exposure images of the same region followed by a post-acquisition image distortion correction and averaging, in which each pixel time was fixed at less than 6 us to avoid the significant beam damage. The ADF-STEM signal was collected at an angle range of 46-200 mrad with an electron beam convergence angle of 24.7 mrad. The occupied sites by Pt atoms were confirmed by comparing the experimental ADF-STEM images and simulated results. The simulation of the ADF-STEM images was performed with the Dr. Probe package[37], and the simulated parameters were fixed based on the experimental conditions. The strain analysis was performed with the geometric phase analysis (GPA) method using a dedicated script for DigitalMicrograph software, in which the strain was calculated with the reference of a perfect MoS_2 lattice.

Device fabrication E-beam lithography (EBL) was used to define a rectangular channel region (2 μm **x** 150 μm) of Pt SMAC/MoS_2 film on SiO_2/Si substrate. The rest Pt SMAC/MoS_2 film was etched away by CHF_3 plasma at -20℃ for 40 s. Ti/Au (5 nm/20 nm) electrodes were defined by the EBL process followed by the e-beam evaporation and lift-off process.

Electrical characterization An Agilent B1500A semiconductor device parameter analyzer was used to examine the transport properties at room temperature in a vacuum chamber of 10^{-2} Torr. Standard DC sweeps are carried out to evaluate the transfer characteristics of all devices.

Ab initio molecular dynamic (MD) simulations for Pt SMACs in ML MoS_2 In this model, the edges are passivated with S atoms. The related calculations were mainly implemented in the Vienna Ab initio Simulation Package (VASP)[38-40], using spin-polarized density functional theory (DFT) based on the generalized gradient approximation (GGA) of the Perdew–Burke–Ernzerhof

(PBE) functional[41]. The core region was described by a projector augmented wave method with a plane-wave kinetic energy cutoff of 500 eV. The vacuum region was set to 15 Å to isolate neighboring periodic images. The Brillouin zone was sampled with a (1 × 20 × 1) *k*-point mesh for geometry optimizations, while a (1 × 30 × 1) mesh was used for electronic structure calculations. The self-consistency convergence criteria for the total energies were set to 10^{-6} eV, and all atomic positions and cell shapes were optimized using the Gaussian smearing method until the force component on each atom is below 0.01 eV $Å^{-1}$. The valences of Mo, S, and Pt were set to 6, 6, and 10, respectively. After structural optimization, the Pt atoms reside in the mirror twin boundary coordinated by 4 adjacent S atoms. The interatomic distance in the chain is 3.19Å. This is very close to the experimental value (3.15Å). For electronic structure calculation, we performed an electronic self-consistent field procedure with tetrahedron method using Blöchl corrections. The thermal stability of Pt SMAC in MoS_2 structure was evaluated by an *ab initio molecular dynamic simulation* using NVT ensemble. The simulation was run at 1000K, and the time step was set to 1fs over 30 ps.

Formation mechanism calculations

The binding energy of a single Pt atom on monolayer MoS_2 To investigate the energy preferred configuration of a single Pt atom on monolayer MoS_2, we calculated the binding energy of Pt atom at different sites of MoS_2. The calculation formula of binding energy is

$$E_b = E_{MoS_2+Pt} - E_{MoS_2} - E_{Pt}$$

where E_{MoS_2+Pt} is the total energy of the system when Pt is adsorbed on MoS_2. E_{MoS_2} is the energy of MoS_2, and E_{Pt} is the energy of a single Pt atom.

Initial structure justification (DFT optimized stable Pt-S_4 configuration) To determine the most stable arrangement of Pt atoms on the MoS_2 edge, we selected 4 representative structures and calculated their average binding energy of Pt-S. The average binding energy is defined as

$$E_{b-aver} = (E_{MoS_2+nPt} - E_{MoS_2} - nE_{Pt})/n$$

Among them, E_{MoS_2+nPt} is the total energy of the system. E_{MoS_2} is the energy of MoS_2 and E_{Pt} is the energy of a single Pt atom, n is the number of Pt atoms.

Electronic properties calculations

Electron localization function (ELF) The local charge density ELF[42, 43] was used to examine the localized characteristics of electrons. Its value is between 0 and 1. The upper limit value 1 means that the electron is completely localized, while 0 means that the electron is completely delocalized. We calculated the local charge density and plotted it. In Fig. 5c, blue represents 0, and red represents 1. It can be found that there is no bond between adjacent Pt atoms, and an electron distribution similar to a covalent bond is formed between S and Pt.

Charge density difference calculation Charge density difference map is generally plotted to view the redistribution of charges after the interaction. Through the calculation and analysis of differential charge density, it is possible to obtain the properties of charge movement and the direction of bonding polarization in the process of bonding and electronic coupling. The definition formula of differential charge density is:

$$\Delta\rho = \rho_{bilayer\ MoS_2} - \rho_{MoS_2-Pt\ layer} - \rho_{MoS_2\ layer}$$

where $\rho_{bilayer\ MoS_2}$ is the charge density of the entire system, $\rho_{MoS_2-Pt\ layer}$ is the charge density of the MoS_2-Pt layer, and $\rho_{MoS_2\ layer}$ is the charge density of the perfect MoS_2 layer. Fig.

5d indicates that charge transfer happens between the Pt atom in the 1st MoS_2 layer and S atoms in the 2nd MoS_2 layer.

Complex-network-based method A representative Pt SMAC inner MoS_2 film of dimension $L \times \frac{L}{2}$ is occupied by a uniformly generated random distribution of Pt SMACs and line defects, and the background MoS_2, as shown in Supplementary Fig. 25b. Widthless Pt SMACs were randomly dispersed in the simulation film with an area density of about 9.4%. We used randomly generated coordinates (x_{Pt}, y_{Pt}) as the center of a Pt SMAC (Note that $0 < x_{Pt} < L, 0 < y_{Pt} < \frac{L}{2}$). Based on our STEM images, we imposed 3-fold symmetry with random overlap for Pt SMACs. Similarly, the line defects were randomly dispersed in the film with an area density of about 10.3%. Random coordinates (x_{defect}, y_{defect}) established the center of the defects and random angle θ with respect to the horizontal direction for its orientation. Then, the generated Pt SMACs inner MoS_2 film was converted into a complex network graph by a universal discretization approach[29]. We assumed line defects as insulators with infinite resistance, background MoS_2 as resistors with resistance 1000 times larger than Pt SMACs. Then we converted the model into a resistor network and implemented the network by Matlab. By solving Kirchhoff's current law and Ohm's law, we calculated the overall resistance and the distribution of current.

Data availability

All data are available in the main text or supplementary materials.

Code availability

The code of the complex-network-based method employed in this work is available at https://doi.org/10.6084/m9.figshare.c.4879863.

Acknowledgements

This work was supported by the support from National Research Foundation Singapore programme NRF-CRP22-2019-0007 and NRF-CRP21-2018-0007. This work is also supported by the Ministry of Education, Singapore, under its AcRF Tier 2 (MOE2019-T2-2-105) and AcRF Tier 1 RG4/17 and RG7/18. This research is also supported by A*STAR under its AME IRG Grant (Project No. A2083c0052). The work at NUAA was supported by the National Key Research and Development Program of China (2019YFA0705400), National Natural Science Foundation of China (11772153, 22073048), the Natural Science Foundation of Jiangsu Province (BK20190018), and a Project by the Priority Academic Program Development of Jiangsu Higher Education Institutions. W.Z. acknowledges the support of the Beijing Outstanding Young Scientist Program (BJJWZYJH01201914430039). B.T. and X.W. acknowledge the support from the Ministry of Education, Singapore (MOE2019 T1-001-113). H.Y. and M. N. acknowledge the support from the Hong Kong Research Grant Council, Hong Kong (HKRGC GRF 12300218, 12300519, 17201020, 17300021, and UGC-RMGS 207300829). H.D. acknowledges the support from German Research Foundation (DFG) under the Grant SFB917 Nanoswitches.

Author contributions

Z.L. and Y.H. guided the project. S.G. and Y.H. synthesized the Pt SMACs. S.G. conducted electronic measurements. J.F. and C.Z. (NTU, SEU) conducted the STEM characterizations. Z.Z. proposed "surf-zip" model. P.Z. and Z.Z. performed the first-principle calculations and analyzed the simulation data. H.Y., M.H., Y.H., and M.N. simulated electronic transport. Z.L., Y.H., Z.Z.,

and C.J. conceived and supervised the experiments. All the authors discussed the results and commented on the manuscript.

Competing interests

We declare no competing financial interests.

Figure Legends/Captions

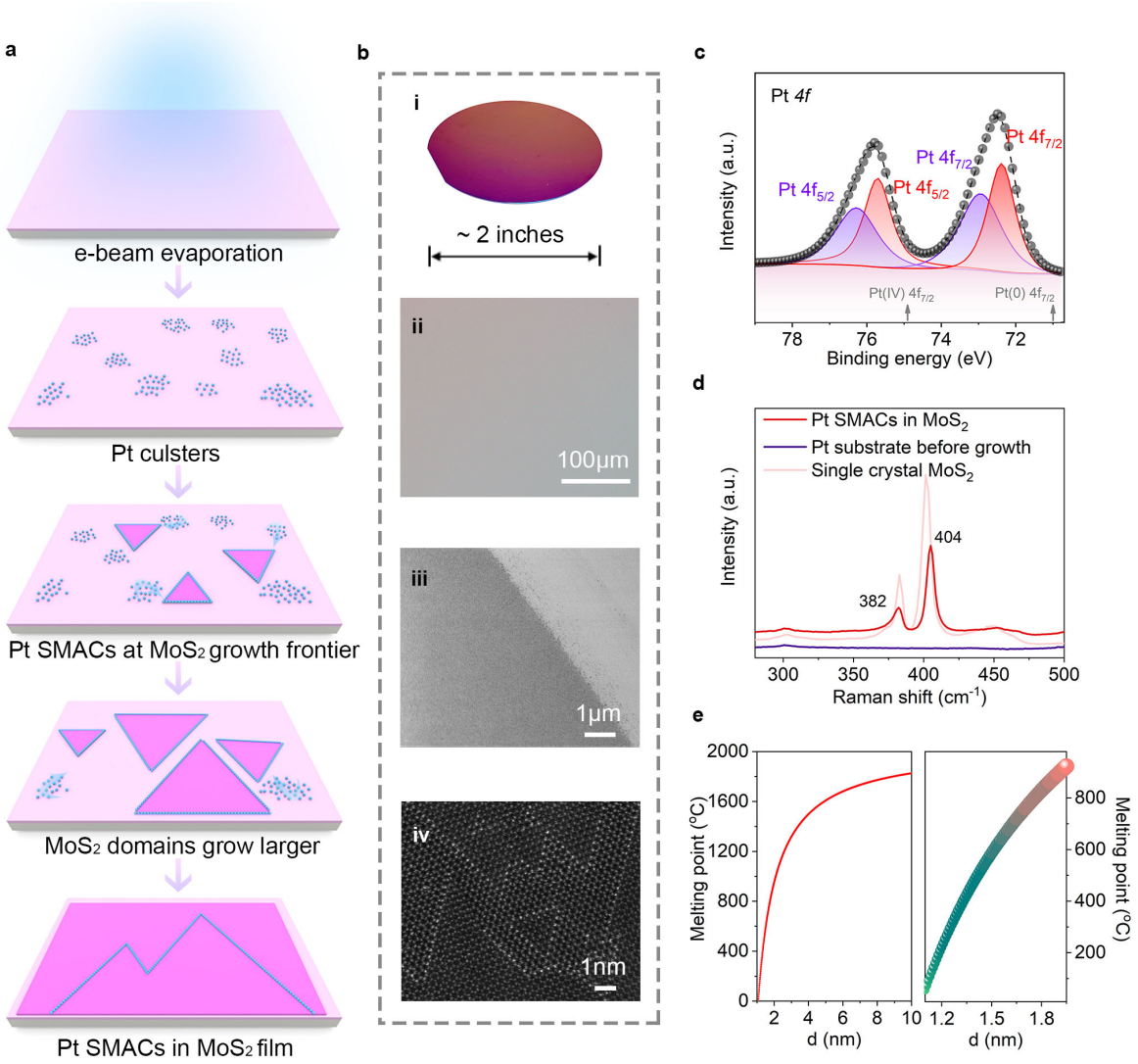

Fig. 1 Growth of Pt SMACs. (**a**) Schematic of the fabrication process with two typical steps: (i) high-density Pt atom-clusters were deposited on a SiO_2/Si substrate by e-beam evaporation at a rate of 0.1 Å s^{-1}, and (ii) Pt SMACs were formed during the growth of MoS_2 films. (**b**) Pt

SMACs/MoS_2 film from wafer-scale to nanoscale, including photograph (i), optical image (ii), SEM image (iii), and atomically resolved ADF-STEM image (iv). The bright dotted lines in (iv) show the contrast of Pt SMACs, and no massive Pt particle is observed in the MoS_2 nanograin film. (**c**) Pt 4f XPS spectra of as-grown film, in which two pairs of peaks were deconvoluted at 72.38, 75.71, 72.94, and 76.28 eV, attributed to the first type of Pt(II) $4f_{7/2}$, the first type of Pt(II) $4f_{5/2}$, the second type of Pt(II) $4f_{7/2}$, and the second type of Pt(II) $4f_{5/2}$, respectively. Grey arrows mark out the location of Pt(0) and Pt(IV). The scatter plot results from fitting the raw data (dashed black line). (**d**) Raman spectra of samples before and after MoS_2 nanograin film growth, and CVD-grown single-crystal MoS_2. (**e**) Left panel, the relationship between the melting point and the diameter for Pt nanoparticles. Right panel, the zoom-in illustration of melting states for clusters with diameter ≤ 2 nm at 650 °C (melted drops in blue and un-melted clusters in red). The clusters with a diameter smaller than 1.56 nm will melt at 650 °C.

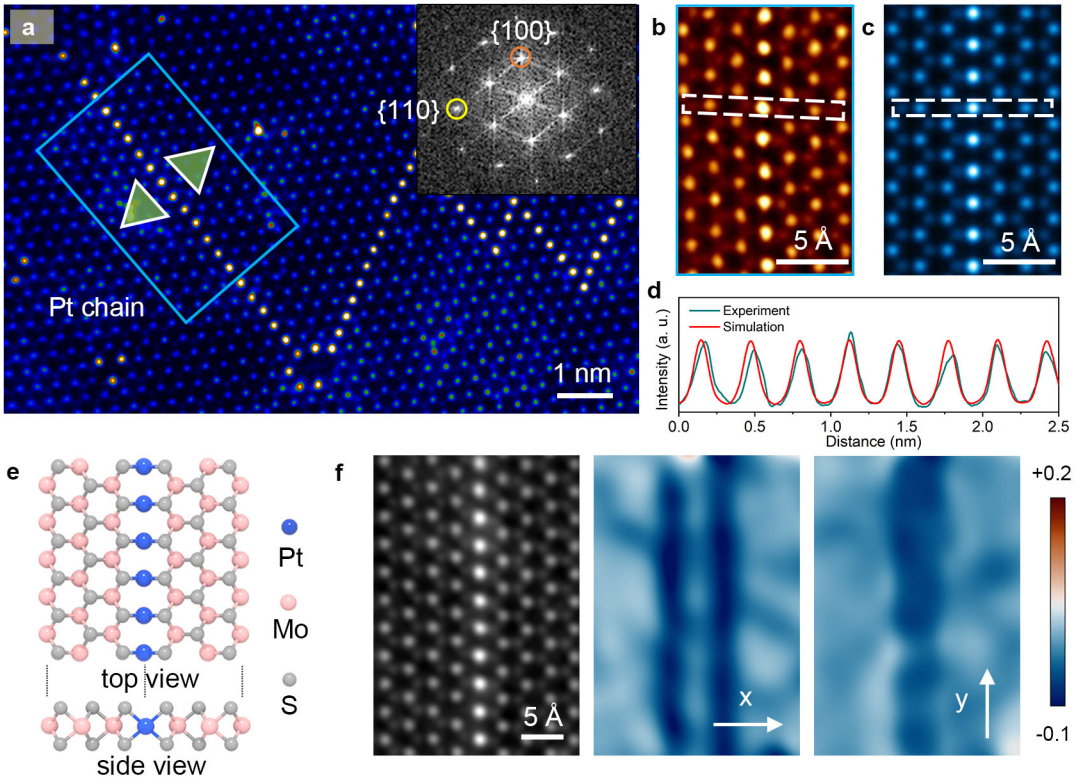

Fig. 2 Atomic structure of Pt SMACs in monolayer MoS_2. (**a**) False-coloured ADF-STEM image of Pt SMACs in monolayer MoS_2. Inset: Fast Fourier transformation (FFT) of the blue rectangular area. (**b**) Magnified ADF-STEM image of a single Pt chain obtained from the blue rectangular in Fig. 2a. (**c**) Simulated ADF-STEM imaging of a Pt chain. (**d**) Intensity profiles of the experimental and simulated images along the Pt SMACs. The average interatomic distance in the chain is measured as 3.2 Å. (**e**) Schematic of the detailed atomic structure of the Pt SMAC in monolayer MoS_2. (**f**) Left panel: magnified ADF-STEM image of a Pt SMAC in monolayer MoS_2. Strain mapping of the left panel with uniaxial strain components ε_{xx} (middle panel) and ε_{yy} (right panel), obtained by geometric phase analysis (GPA).

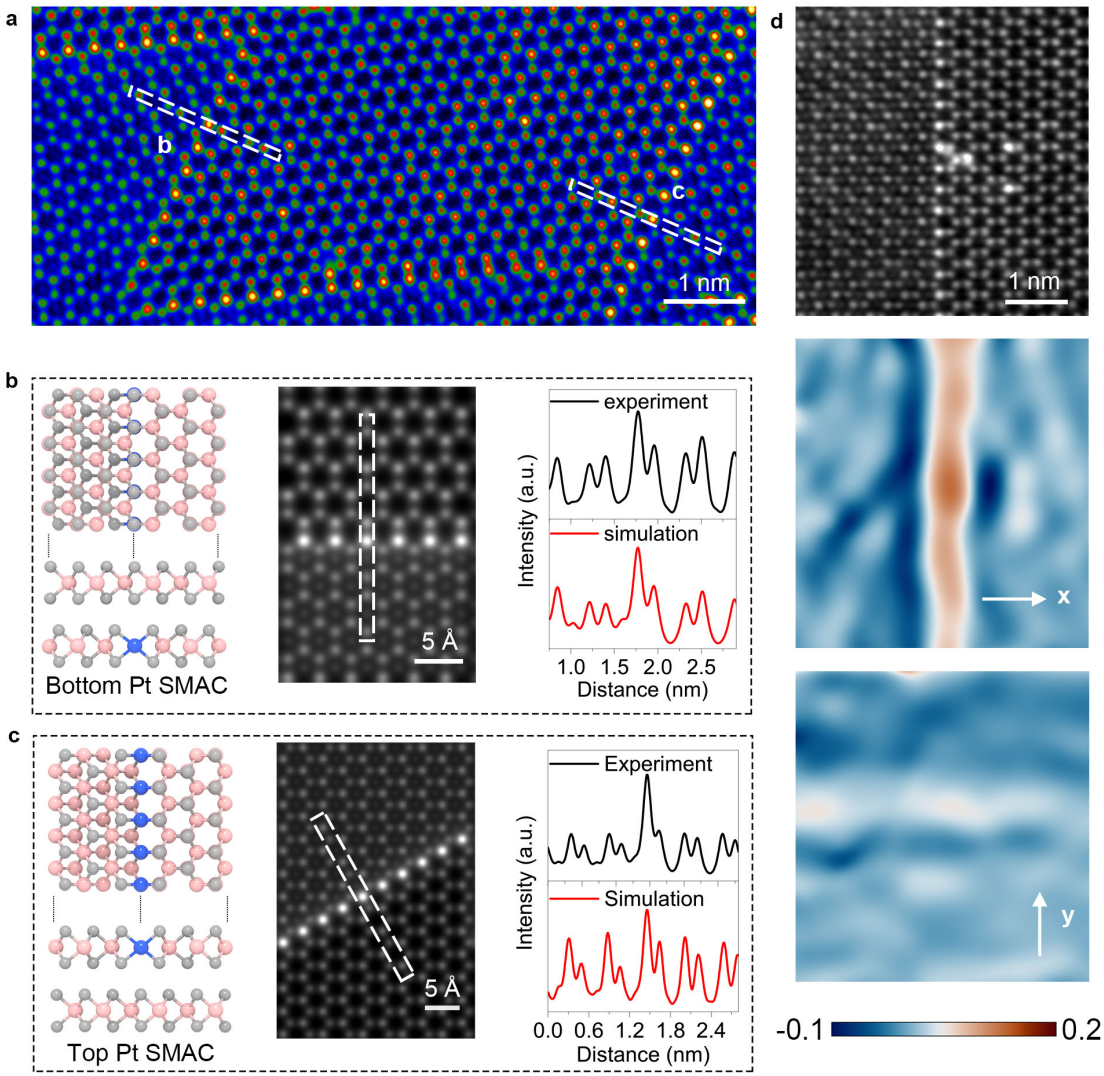

Fig. 3 Atomic structure of Pt SMACs in bilayer MoS_2. (**a**) False-colored ADF-STEM image of a bilayer MoS_2 region. (**b**) Atomic structure of Pt SMACs in the bottom layer of MoS_2, as shown with structural schematic (left), simulated STEM image (middle), and intensity profiles (right) along the white dashed box in Fig. 3a and the corresponding simulated STEM image. (**c**) Atomic structure of Pt SMACs in the top layer of MoS_2, as shown with structural schematic (left), simulated STEM image (middle), and intensity profiles (right) along the white dashed box in Fig. 3a and the corresponding simulated STEM image. (**d**) Top panel: magnified ADF-STEM image of a Pt SMAC in bilayer MoS_2. Strain mapping of the Pt SMAC in bilayer MoS_2, including ε_{xx} strain (middle) and ε_{yy} strain (bottom).

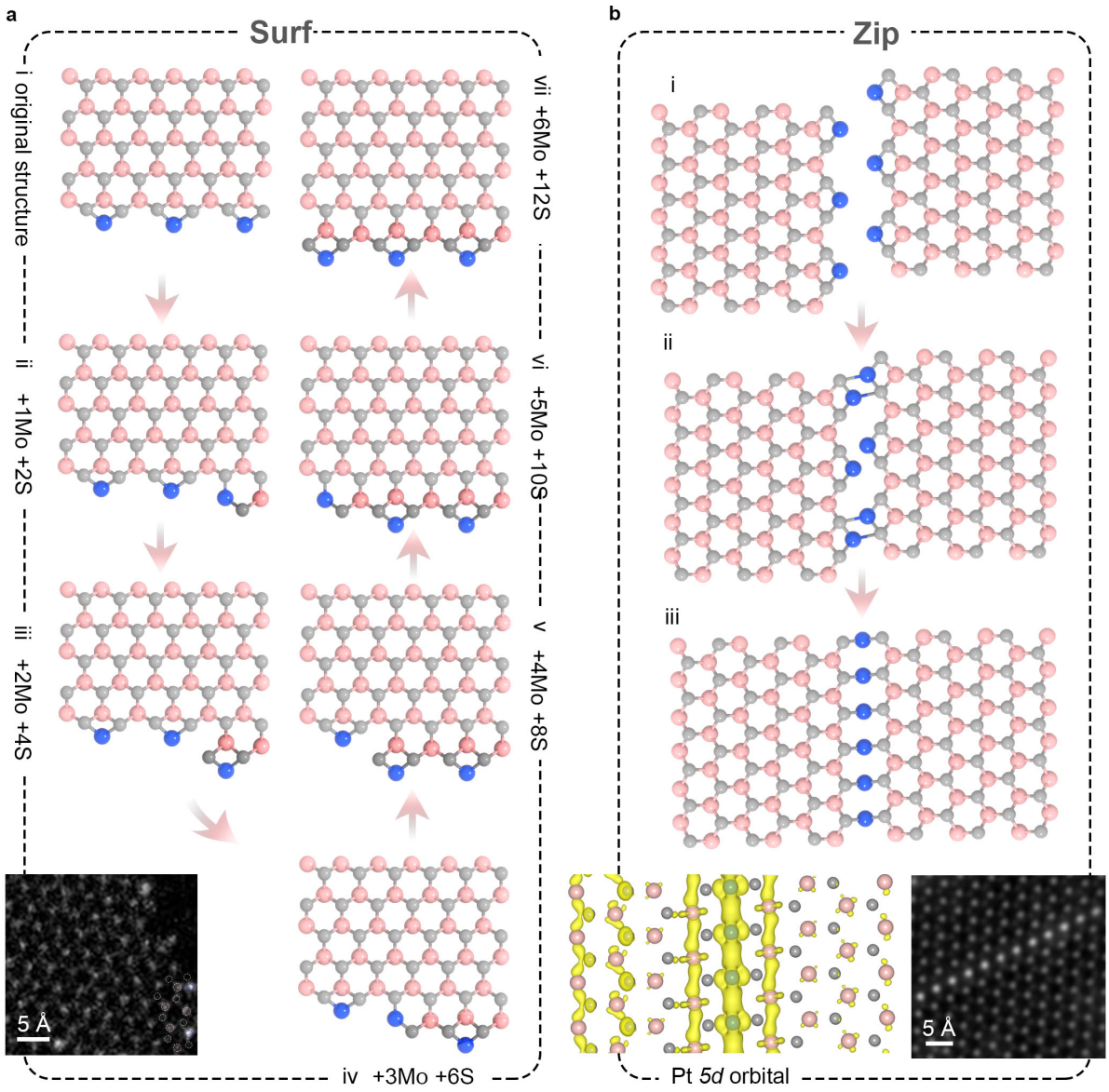

Fig. 4 Formation mechanism of Pt SMACs. (**a**) Energetically optimal atomic configurations i-vii during the step-by-step addition of MoS_2 units to a Pt-passivated zigzag edge. The feeding species for each step is Mo+2S. The growth leads to kink movement, shifting Pt atoms as if they surf along the growth front by coming feeding species. The bottom STEM image presents the evidence of the lowest energy intermediate state (iv). (**b**) The formation of Pt SMACs. Pt atoms along two zigzag edges zip together (ii, iii) when two inversely oriented Pt terminated MoS_2 domains meet each other. The STEM image corresponds to the formation of a complete Pt SMAC. The inset is isosurface plots (0.033776 e/ $Å^3$) of the partial charge density distribution of Pt 5*d* orbitals. A substantial overlap of electron densities between adjacent Pt atoms can be well-identified.

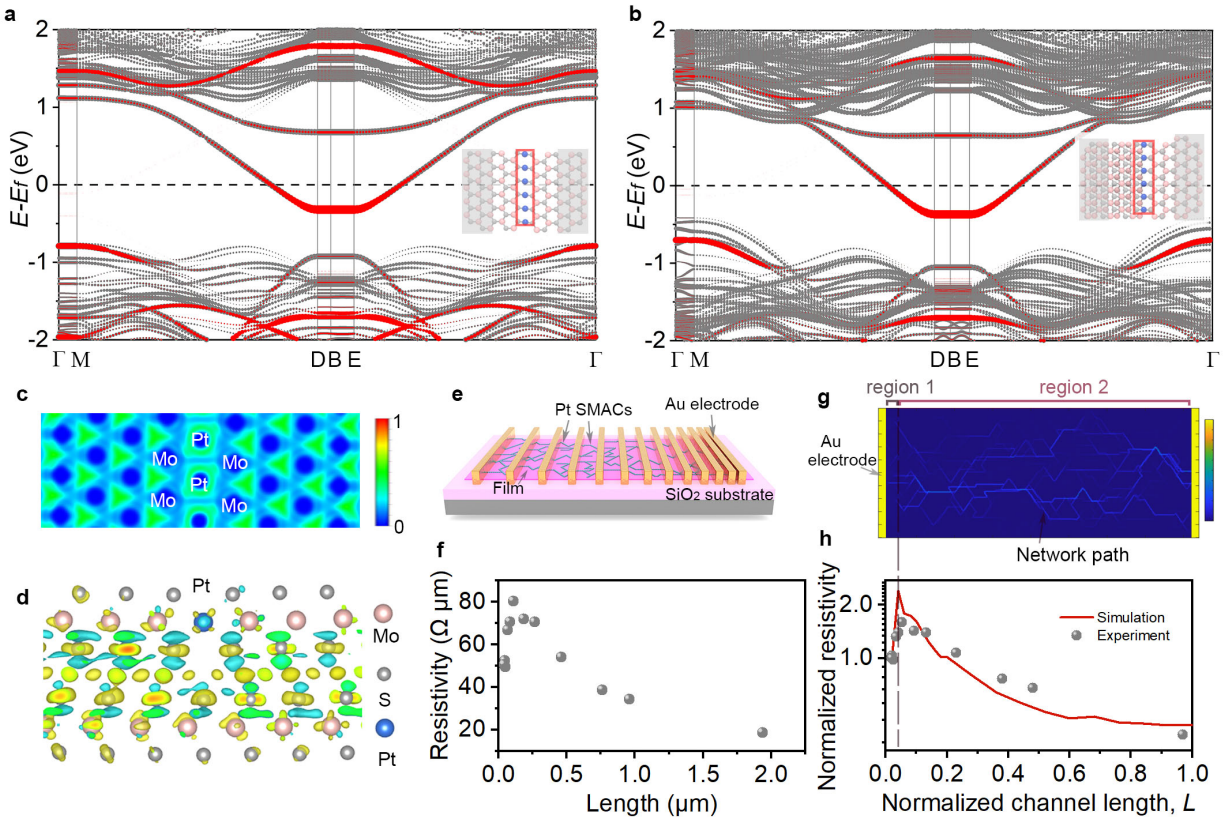

Fig. 5 Electronic structure of Pt SMAC. (**a, b**) Electronic band structures of a Pt SMAC embedded in a monolayer (a) and bilayer (b) MoS_2, respectively. The band structures are projected onto just the Pt atoms as well as those atoms in the bulk area (unshaded regions in the atomic structure). The weight character of bands is thickness encoded. Red lines mark the contribution of the Pt plus the S atoms directly bonded to them. The grey lines represent the whole Pt SMACs/MoS_2 system. (**c**) Electron localization function (ELF) map of Pt SMACs in a monolayer MoS_2 on the (001) pane. There is only weak electronic localization between adjacent Pt atoms. (**d**) Isosurface plot (*0.00016 e/Å*^{3}) of charge density difference between a SMAC-containing MoS_2 layer and a pristine MoS_2 layer (side view). The charge accumulation and depletion regions are distinguished by yellow and blue, respectively. (**e**) Schematic illustration of transmission-line model (TLM) devices. The device structures with channel lengths from 2 μm to 50 nm are fabricated, and the channel width is defined to be 1μm. (**f**) Room temperature resistivity as a function of channel length extracted using a typical two-terminal TLM. (**g**) Current color map calculated for the device with the largest channel length of *L* (normalized value of 1, corresponding to 2 μm in the experiment). (**h**) Normalized simulated resistivity and experimental results versus channel length.

References

1. Li, H. et al. Synergetic interaction between neighbouring platinum monomers in CO_2 hydrogenation. *Nat. Nanotechnol.* **13**, 411-417 (2018).
2. Ahn, J., Yeom, H., Yoon, H. & Lyo, I.-W. Metal-insulator transition in Au atomic chains on Si with two proximal bands. *Phys. Rev. Lett.* **91**, 196403 (2003).
3. Gambardella, P. *et al.* Ferromagnetism in one-dimensional monatomic metal chains. *Nature* **416**, 301-304 (2002).
4. Pham, T. et al. Torsional instability in the single-chain limit of a transition metal trichalcogenide. *Science* **361**, 263-266 (2018).
5. Dua, P., Lee, G. & Kim, K. S. Ferromagnetism in monatomic chains: Spin-dependent bandwidth narrowing/broadening. *J. Phys. Chem. C* **121**, 20994-21000 (2017).
6. Bergman, A., Hellsvik, J., Bessarab, P. F. & Delin, A. Spin relaxation signature of colossal magnetic anisotropy in platinum atomic chains. *Sci. Rep.* **6**, 36872 (2016).
7. Rubio-Bollinger, G., Bahn, S. R., Agrait, N., Jacobsen, K. W. & Vieira, S. Mechanical properties and formation mechanisms of a wire of single gold atoms. *Phys. Rev. Lett.* **87**, 026101 (2001).
8. Ohnishi, H., Kondo, Y. & Takayanagi, K. Quantized conductance through individual rows of suspended gold atoms. *Nature* **395**, 780-783 (1998).
9. Kizuka, T. Atomic configuration and mechanical and electrical properties of stable gold wires of single-atom width. *Phys. Rev. B* **77**, 155401 (2008).
10. Sokolov, A., Zhang, C., Tsymbal, E. Y., Redepenning, J. & Doudin, B. Quantized magnetoresistance in atomic-size contacts. *Nat. Nanotechnol.* **2**, 171-175 (2007).
11. Autès, G., Barreteau, C., Desjonquères, M. C., Spanjaard, D. & Viret, M. Giant orbital moments are responsible for the anisotropic magnetoresistance of atomic contacts. *Europhys Lett* **83**, 17010 (2008).
12. Calvo, M. R. et al. The Kondo effect in ferromagnetic atomic contacts. *Nature* **458**, 1150-1153 (2009).
13. Oncel, N. Atomic chains on surfaces. *J. Phys.: Condens. Matter* **20**, 393001 (2008).
14. Snijders, P. C. & Weitering, H. H. Colloquium: Electronic instabilities in self-assembled atom wires. *Reviews of Modern Physics* **82**, 307-329 (2010).
15. Blumenstein, C. et al. Atomically controlled quantum chains hosting a Tomonaga–Luttinger liquid. *Nat. Phys.* **7**, 776-780 (2011).
16. Yanson, A., Bollinger, G. R., Van den Brom, H., Agrait, N. & Van Ruitenbeek, J. Formation and manipulation of a metallic wire of single gold atoms. *Nature* **395**, 783-785 (1998).
17. Lehtinen, O. et al. Atomic scale microstructure and properties of Se-deficient two-dimensional $MoSe_2$. *ACS Nano* **9**, 3274-3283 (2015).
18. Ma, Y. et al. Angle resolved photoemission spectroscopy reveals spin charge separation in metallic $MoSe_2$ grain boundary. *Nat. Commun.* **8**, 14231 (2017).
19. Zhou, W. et al. Intrinsic structural defects in monolayer molybdenum disulfide. *Nano Lett.* **13**, 2615-2622 (2013).
20. Ma, Y. et al. Metallic twin grain boundaries embedded in $MoSe_2$ monolayers grown by molecular beam epitaxy. *ACS Nano* **11**, 5130-5139 (2017).
21. Nanda, K. K., Sahu, S. N. & Behera, S. N. Liquid-drop model for the size-dependent melting of low-dimensional systems. *Phys. Rev. A* **66**, 013208 (2002).
22. Voiry, D. et al., The role of electronic coupling between substrate and 2D MoS_2 nanosheets in electrocatalytic production of hydrogen. *Nat. Mater.* **15**, 1003-1009 (2016).

23. Vancsó, P. et al. The intrinsic defect structure of exfoliated MoS_2 single layers revealed by Scanning Tunneling Microscopy. *Sci. Rep.* **6,** 29726 (2016).24. Fu, Y., Rudnev, A. V., Wiberg, G. K. & Arenz, M. Single graphene layer on Pt (111) creates confined electrochemical environment via selective ion transport. *Angew. Chem. Int. Ed.* **56**, 12883-12887 (2017).
25. Xu, S. et al., Direct Integration of Strained-Pt Catalysts into Proton-Exchange-Membrane Fuel Cells with Atomic Layer Deposition. *Adv. Mater*. 33, 2007885 (2021).
26. Xia, M. et al. Spectroscopic signatures of AA′ and AB stacking of chemical vapor deposited bilayer MoS_2. *ACS Nano* **9**, 12246-12254 (2015).
27. Liu, H. et al., Switching mechanism in single-layer molybdenum disulfide transistors: An insight into current flow across Schottky barriers. *ACS Nano* 8, 1031-1038 (2014).
28. Jin, G. et al. Atomically thin three-dimensional membranes of van der Waals semiconductors by wafer-scale growth. *Sci. Adv.* **5**, eaaw3180 (2019).
29. Yao, H., Hsieh, Y.-P., Kong, J. & Hofmann, M. Modelling electrical conduction in nanostructure assemblies through complex networks. *Nat. Mater* **19**, 745-751 (2020).
30. Albert, R. & Barabási, A.-L. Statistical mechanics of complex networks. *Rev. Mod. Phys.* **74**, 47-97 (2002).
31. Lee, D., Kahng, B., Cho, Y. S., Goh, K. I. & Lee, D. S. Recent Advances of Percolation Theory in Complex Networks. *J Korean Phys Soc* **73**, 152-164 (2018).
32. Yao, H., Hempel, M., Hsieh, Y.-P., Kong, J. & Hofmann, M. Characterizing percolative materials by straining. *Nanoscale* **11**, 1074-1079 (2019).
33. Jolie, W. et al. Tomonaga-Luttinger liquid in a box: electrons confined within MoS_2 mirror-twin boundaries. *Phys. Rev. X* **9**, 011055 (2019).
34. Barja, S. et al. Charge density wave order in 1D mirror twin boundaries of single-layer $MoSe_2$. *Nat. Phys.* **12**, 751-756 (2016).
35. Nagao, T., Yaginuma, S., Inaoka, T. & Sakurai, T. One-dimensional plasmon in an atomic-scale metal wire. *Phys. Rev. Lett.* **97**, 116802 (2006).
36. Segovia, P., Purdie, D., Hengsberger, M. & Baer, Y. Observation of spin and charge collective modes in one-dimensional metallic chains. *Nature* **402**, 504-507 (1999).
37. Barthel, J. Dr. Probe: A software for high-resolution STEM image simulation. *Ultramicroscopy* **193**, 1-11 (2018)
38. Kresse, G. & Hafner, J. Ab initio molecular dynamics for liquid metals. *Phys. Rev. B* **47**, 558 (1993).
39. Kresse, G. & Furthmüller, J. Efficiency of ab-initio total energy calculations for metals and semiconductors using a plane-wave basis set. *Comput. Mater. Sci.* **6**, 15-50 (1996).
40. Kresse, G. & Hafner, J. Ab initio molecular-dynamics simulation of the liquid-metal–amorphous-semiconductor transition in germanium. Phys. Rev. B **49**, 14251-14269 (1994).
41. Perdew, J. P., Burke, K. & Ernzerhof, M. Generalized gradient approximation made simple. *Phys. Rev. Lett.* **77**, 3865 (1996).
42. Silvi, B. & Savin, A. Classification of chemical bonds based on topological analysis of electron localization functions. *Nature* **371**, 683-686 (1994).
43. Savin, A., Nesper, R., Wengert, S. & Fässler, T. F. ELF: The electron localization function. *Angew Chem. Int. Ed. Engl.* **36**, 1808-1832 (1997).